Supplement of Atmos. Chem. Phys., 26, 16895–16916, 2026
https://doi.org/10.5194/acp-26-16895-2026-supplement
© Author(s) 2026. CC BY 4.0 License.



Atmospheric Chemistry and Physics
Open Access
EGU

Supplement of

Drivers of aerosol variability in the high Arctic: insights from integrated observations at Gruvebadet and Zeppelin (Ny-Ålesund)

Elena Barbaro et al.

Correspondence to: Matteo Feltracco (matteo.feltracco@unive.it)

The copyright of individual parts of the supplement might differ from the article licence.

S1.1 Meteorological and radiation data

Key meteorological variables, such as air temperature, relative humidity, atmospheric pressure, wind speed and direction, and stability parameters (Fig. S1), but also solar (shortwave) radiation, net longwave radiation and surface albedo were evaluated (Fig. S2). Daily values are shown with time series, while the wind rose and histogram for stability parameters were generated with 30- minute averages.

Daily temperatures fluctuated between -25°C and +25°C, staying below zero from winter to spring and rising in summer. Wind speeds mostly remained under 10 m s^{-1}, with a dominant E-SW pattern aligned with Kongsfjorden. Notably, Mazzola et al. (2016) observed similar statistical distributions for wind components during summer.The stability parameter z/L shifted from positive (stable) to negative (unstable) values during summer, a behavior strictly linked to snow-free ground between June and October (Becherini et al., 2021). Snow cover increases albedo and limits heating, promoting stability, while snow-free soil enhances solar absorption and vertical mixing. Figure S1c confirms that >50% of Obukhov length values are positive. Radiative data showed solar peaks exceeding 350 W m^{-2} in spring/summer, dropping to zero during the polar night. Net longwave flux remained mostly negative, indicating winter radiative cooling, though clouds or inversions caused occasional positive shifts. Surface albedo decreased from 0.9 (snow-covered) to below 0.3 in summer as tundra or water became exposed.

The polar plot reported in Fig. S3 shows that the highest aerosol absorption coefficient values ($\sigma abs > 2.0$ Mm-1, dark red markers) are predominantly associated with winds coming from the North (345° - 360°) and East/South-East (90° - 110°) sectors at moderate to high wind speeds (5 - 12 m/s). These high-absorption events also correspond to smaller marker sizes, which signify lower Single Scattering Albedo values (SSA $\cong$ 0.85) and point to the presence of strongly absorbing anthropogenic aerosols such as black carbon. Interestingly, the North-East sector (45°)—where the human settlement is located just 1 km away—exhibits low data density and significantly lower absorption levels, indicating that direct pollution transport from this nearby settlement is not the primary driver of contamination at the measurement site; instead, the main sources of contamination appear to originate from the Northern and Eastern/South-Eastern sectors or are transported from farther upwind sources.

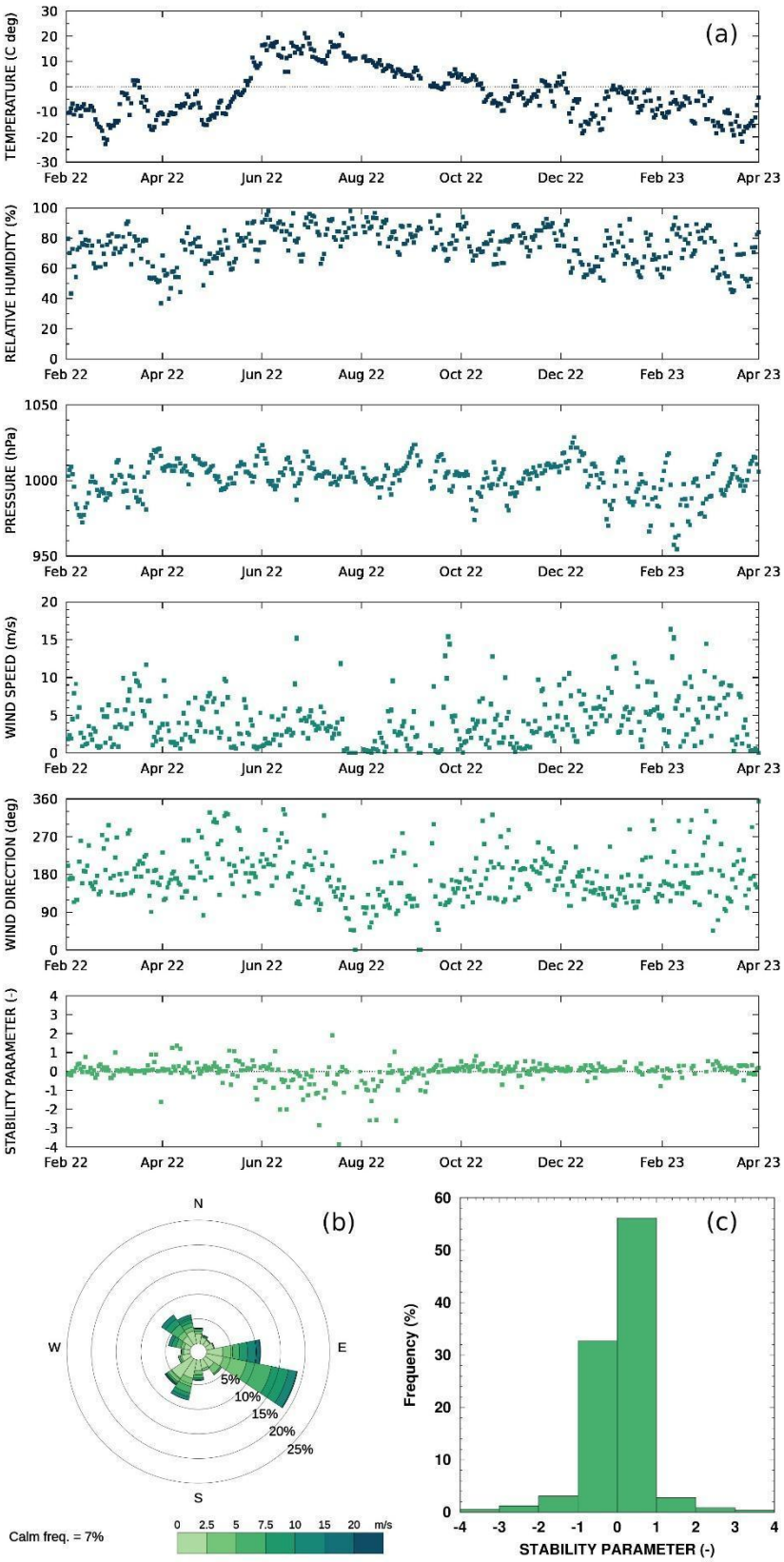


Figure S1. (a) Time series of daily values of meteorological and stability parameters measured at CCT during the study period. (b) Polar plot of the wind patterns. (c) Frequency histogram of the stability parameter. Plots in (b) and (c) were obtained using 30-minute values.

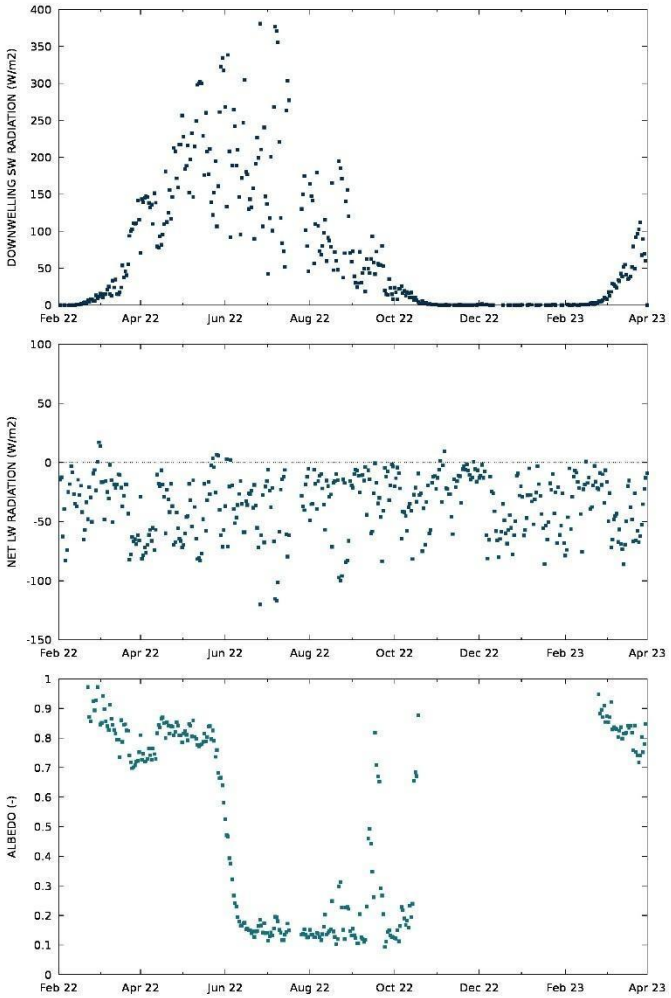


Figure S2. Time series of daily values of solar radiation (upper panel), net longwave radiation (middle panel) and surface albedo (lower panel) measured at CCT during the study period.

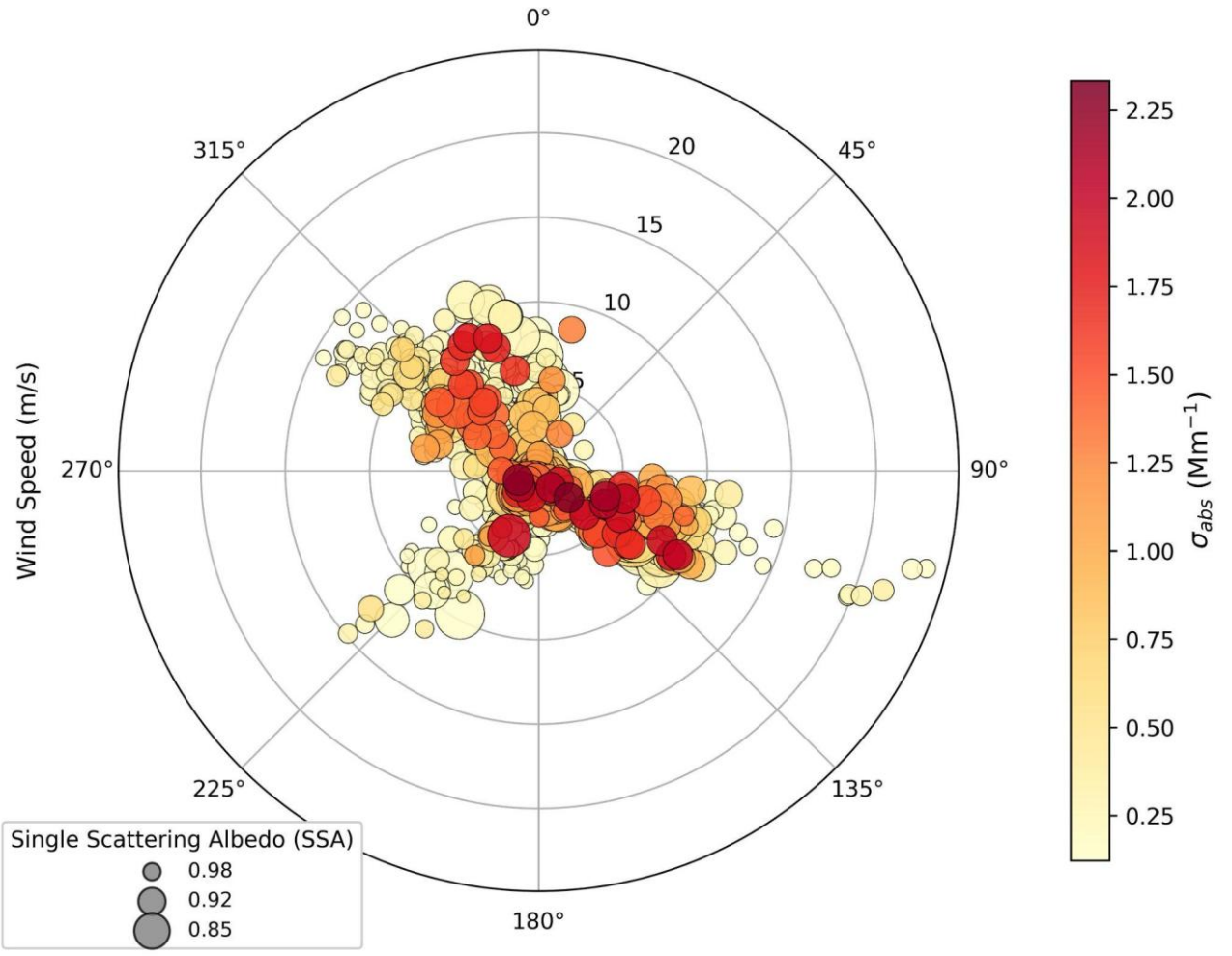


Figure S3. Aerosol absorption coefficient (σabs) and Single Scattering Albedo (SSA) as a function of wind direction and wind speed.

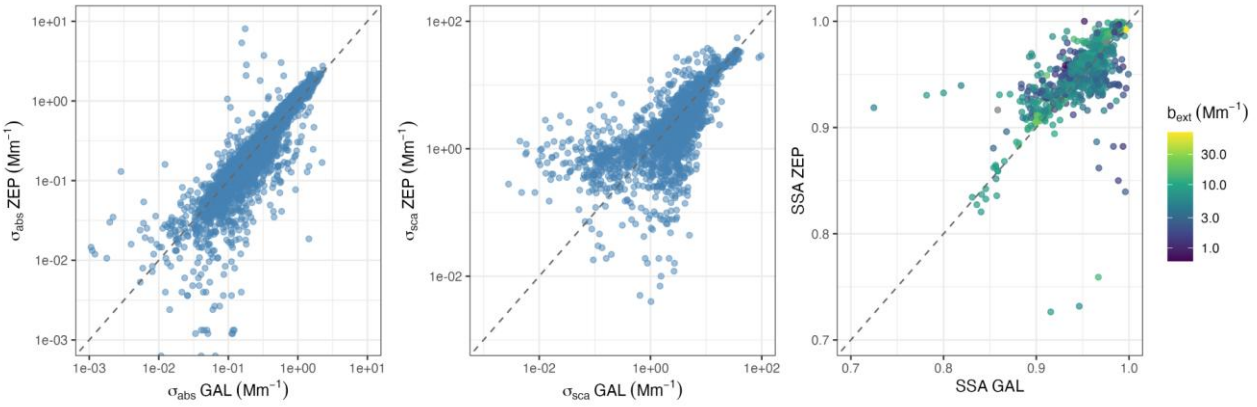


Figure S4. Comparison between absorption coefficients, scattering coefficients, and single scattering albedo at the two sites. SSA markers are color-coded as a function of the mean extinction coefficients.

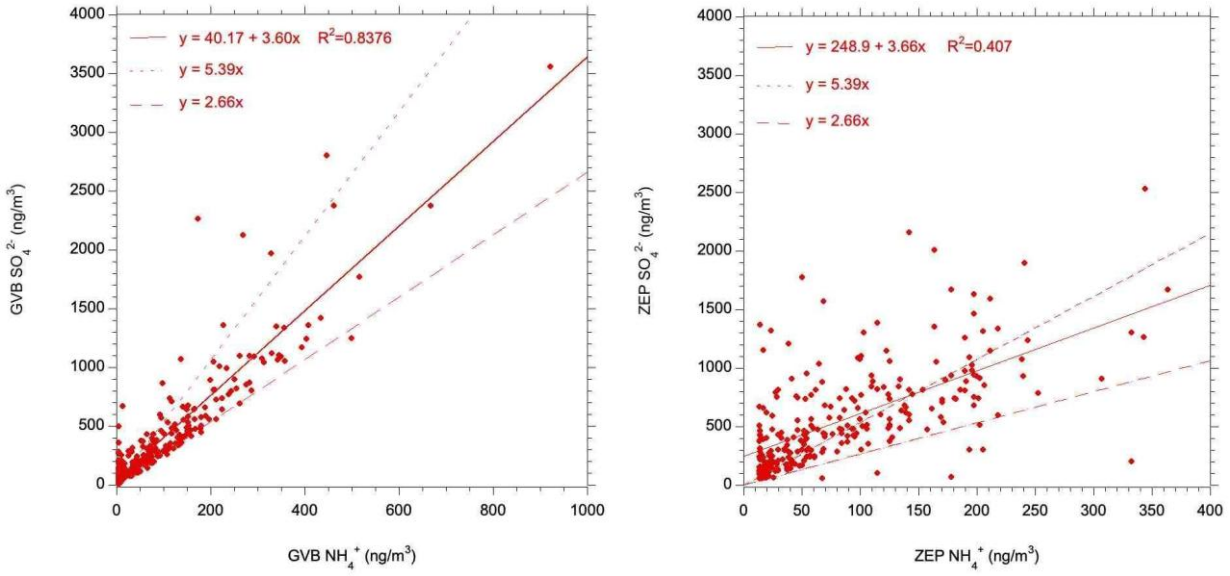


Figure S5. Linear correlation between sulphate and ammonium obtained using the entire dataset from Jan 2022 to Jun 2023 at GAL and ZEP.

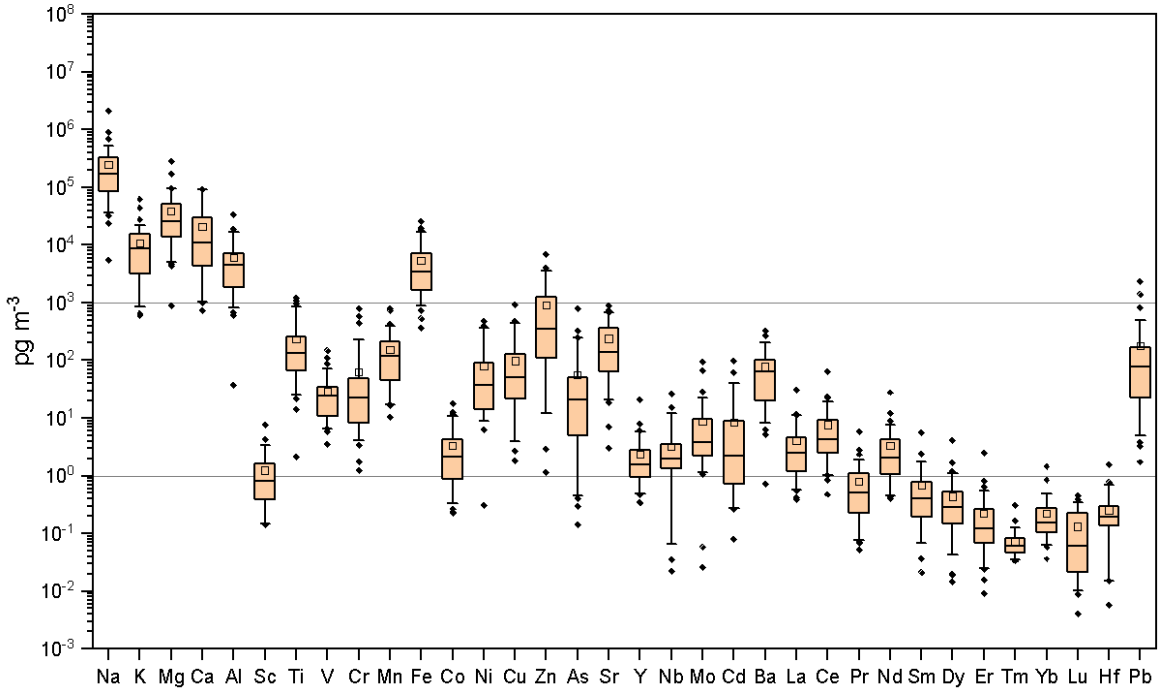


Figure S6. Boxplot for the mass concentration in air of the elements monitored in the PM_{10} samples. The extremes of the whiskers point to the 5th and 95th percentile of each distribution.

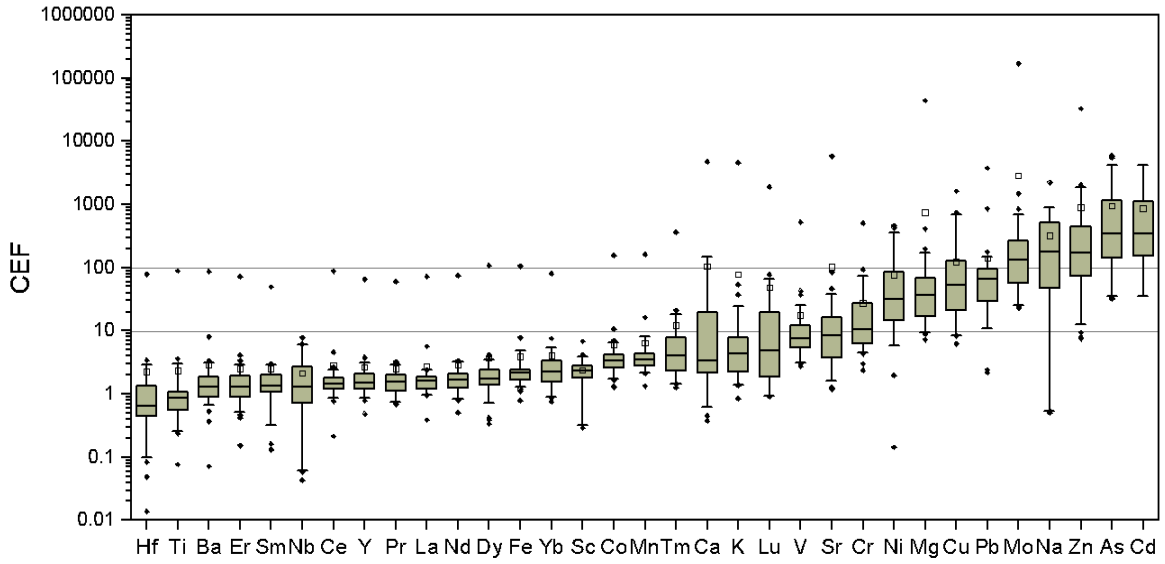


Figure S7. Boxplot for the crustal enrichment factors. The elements are sorted by increasing median order. The extremes of the whiskers point the 5th and 95th percentile of each distribution.

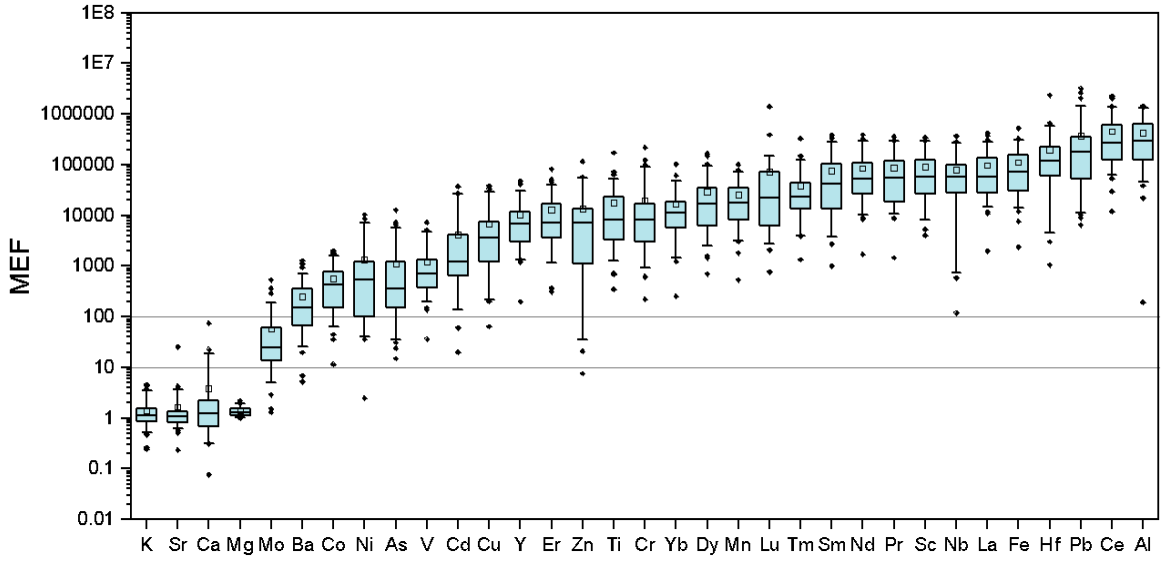


Figure S8. Boxplot for the marine enrichment factors. The elements are sorted by increasing median order. The extremes of the whiskers point to the 5th and 95th percentile of each distribution.

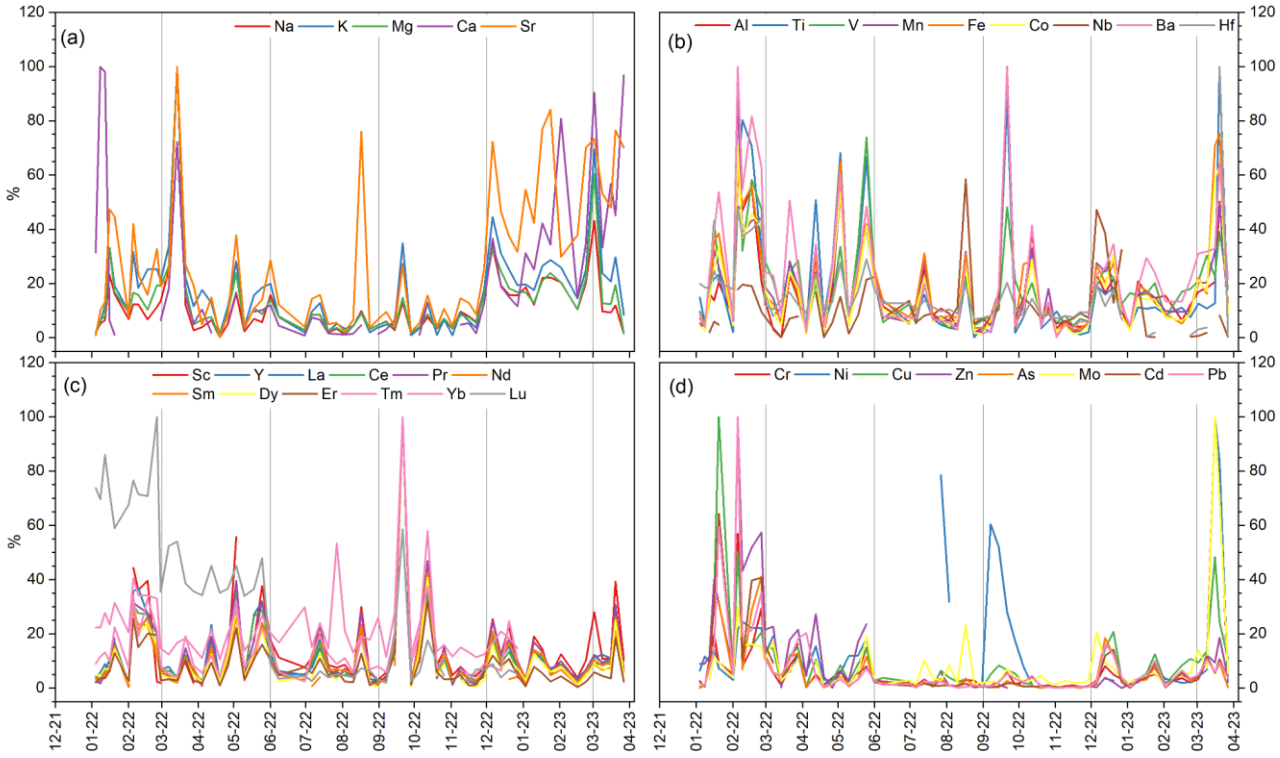


Figure S9. Normalized temporal profiles of the analysed elements. For each element, concentrations were divided by the maximum value observed for that element over the study period and expressed as a percentage. The elements are grouped according to their value of CEF and MEF, which define the specific sources: a) marine, b) and c) crustal, and d) anthropogenic sources.

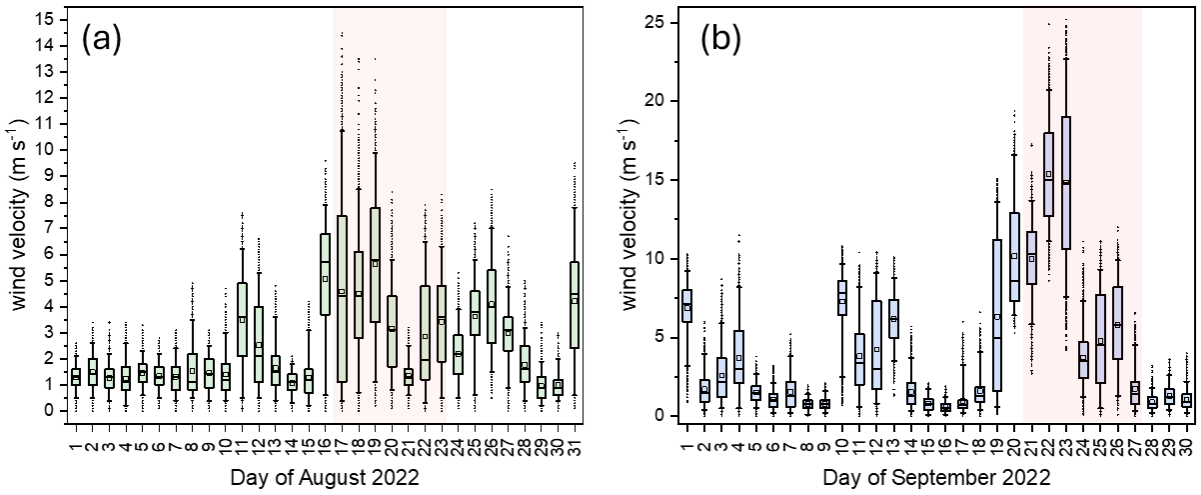


Figure S10. Boxplot for the wind velocity for each day of August and September 2022. The extremes of the whiskers point the 5th and 95th percentile of each distribution.

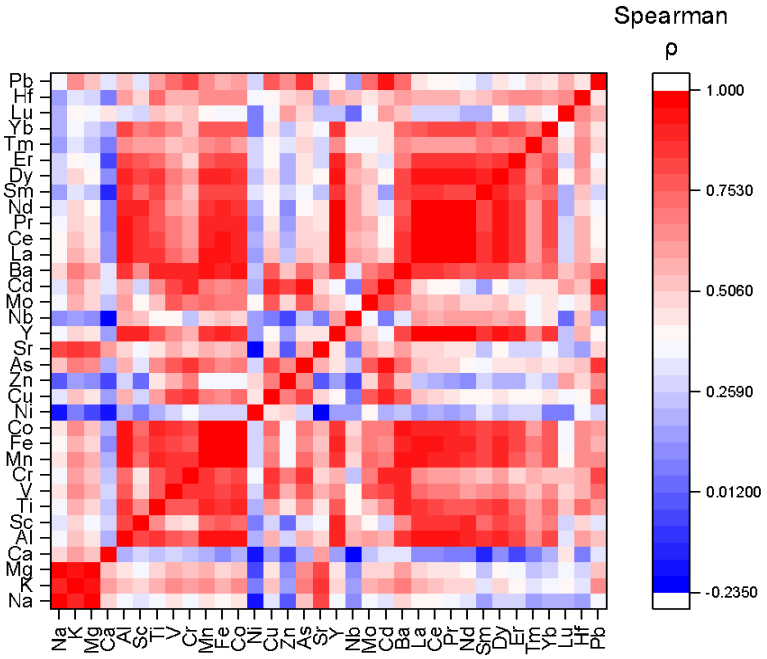


Figure S11. Spearman's ρ correlation coefficient for the concentration of the elements normalized for the relative maximum value.

Table S1. Median and interquartile range for the season mass concentration for PM_{10} samples collected from January 2022 to March 2023 at Gruvebadet atmosphere laboratory and Zeppelin observatory (ng m^{-3}).

		Winter	Spring	Summer	Autumn
Al	GAL	5.4 (3.6)	6.1 (8.0)	3.3 (3.0)	2.2 (2.9)
	ZEP	53.1(50.3)	31.4(22.4)	21.7 (44.6)	64.3(95.5)
As	GAL	0.05 (0.11)	0.03 (0.06)	0.01 (0.01)	0.003 (0.004)
	ZEP	0.03 (0.11)	0.04 (0.05)	0.007 (0.012)	0.02 (0.02)
Cd	GAL	0.01 (0.02)	0.007 (0.006)	0.001 (0.001)	0.0006 (0.0002)
	ZEP	0.03 (0.03)	0.012 (0.007)	0.01 (0.08)	0.005 (0.019)
Cr	GAL	0.04 (0.06)	0.04 (0.07)	0.02 (0.01)	0.01 (0.01)
	ZEP	0.31 (0.27)	0.18 (0.12)	0.24 (0.22)	0.41 (0.30)
Co	GAL	0.003 (0.004)	0.004 (0.003)	0.001 (0.001)	0.001 (0.002)
	ZEP	0.013 (0.007)	0.010(0.006)	0.004(0.00725)	0.014(0.021)
Cu	GAL	0.09 (0.12)	0.1 (0.1)	0.03 (0.01)	0.02 (0.04)
	ZEP	0.26 (0.20)	0.17 (0.20)	0.07 (0.08)	0.21 (0.46)
Fe	GAL	4.3 (5.1)	5.8 (5.5)	2.1 (2.3)	1.6 (3.0)
	ZEP	20.3 (15.5)	14.1 (12.0)	6.1 (5.6)	28.7 (38.9)
Pb	GAL	0.16 (0.28)	0.12 (0.15)	0.03 (0.03)	0.01 (0.04)
	ZEP	0.16 (0.54)	0.19 (0.18)	0.05 (0.05)	0.11 (0.10)
Mn	GAL	0.13 (0.15)	0.12 (0.13)	0.06 (0.05)	0.04 (0.09)
	ZEP	0.46 (0.30)	0.38 (0.34)	0.20 (1.05)	0.54 (1.02)
Ni	GAL	0.03 (0.05)	0.03 (0.05)	0.01 (0.14)	0.11 (0.17)
	ZEP	0.15 (0.19)	0.09 (0.11)	0.09 (0.02)	0.12 (0.19)
Ti	GAL	0.19 (0.14)	0.15 (0.25)	0.08 (0.13)	0.06 (0.09)
	ZEP	1.83 (2.345)	1.29 (0.81)	0.64 (0.58)	2.42 (3.14)
V	GAL	0.03 (0.02)	0.03 (0.02)	0.01 (0.01)	0.01 (0.01)
	ZEP	0.07 (0.04)	0.06 (0.06)	0.02 (0.02)	0.09 (0.09)
Zn	GAL	0.5 (1.8)	0.6 (1.0)	0.1 (0.2)	0.07 (0.04)
	ZEP	1.6 (2.3)	1.4 (1.1)	0.4 (2.2)	0.8 (3.2)

Table S2. Summary of the results for Pb concentration, isotope ratio values, and crustal enrichment factors (CEFs) for PM_{10} samples collected at GAL from February 2022 to March 2023 (n = 58).

Statistics	Pb (pg/m^3)	CEF	$^{208}Pb/^{206}Pb$	$^{207}Pb/^{206}Pb$
Mean	174	127	2.102	0.861
SD	287	157	0.010	0.005
Min	4.4	5.9	2.073	0.848
Q1	21	35	2.096	0.859
Median	80	69	2.103	0.861
Q3	191	149	2.108	0.863
Max	1823	778	2.119	0.874
IQR	170	114	0.012	0.004

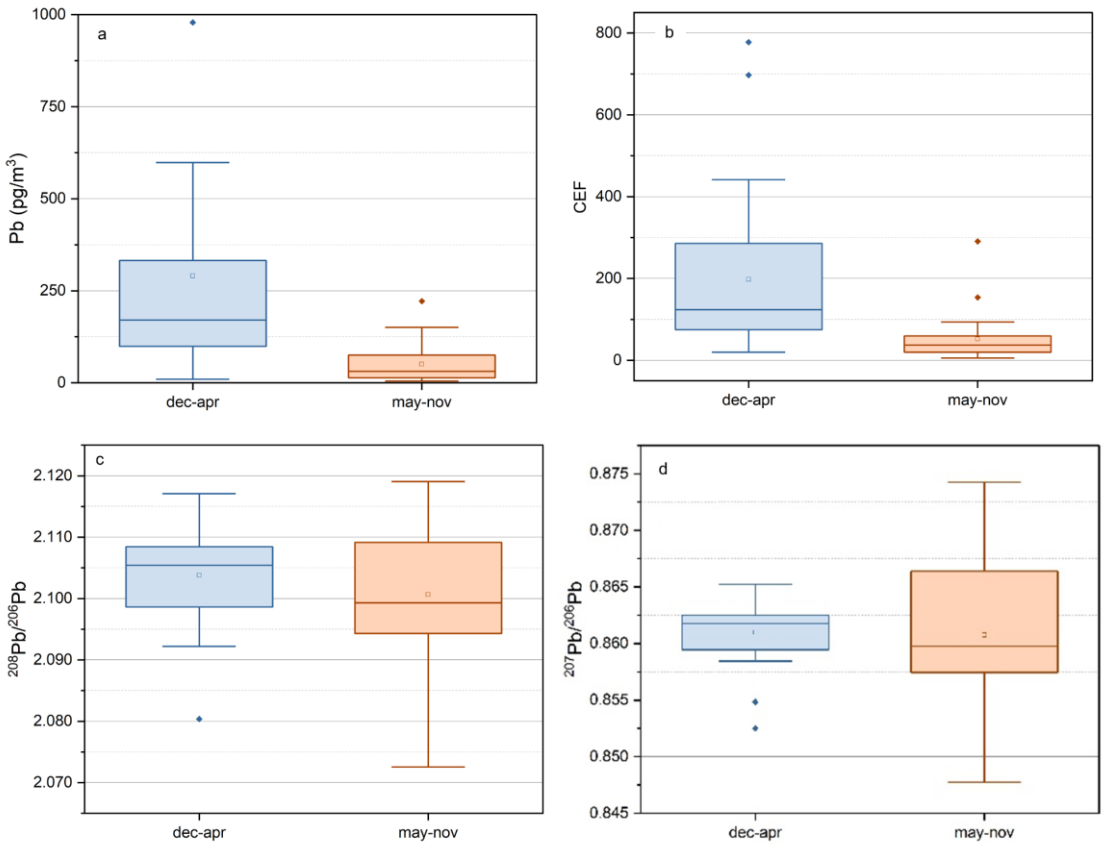


Fig. S12. Boxplot representation of Pb data. a) Pb concentration, b) CEF, c) $^{208}Pb/^{206}Pb$ and d) $^{207}Pb/^{206}Pb$. Each box is delimited by 25th and 75th percentiles; thick line represents the median, whiskers indicate the minimum and maximum values within 1.5 interquartile range, and dots are values outside the whiskers (outliers).



Fig. S13. Enrichment factor of silicon**.**

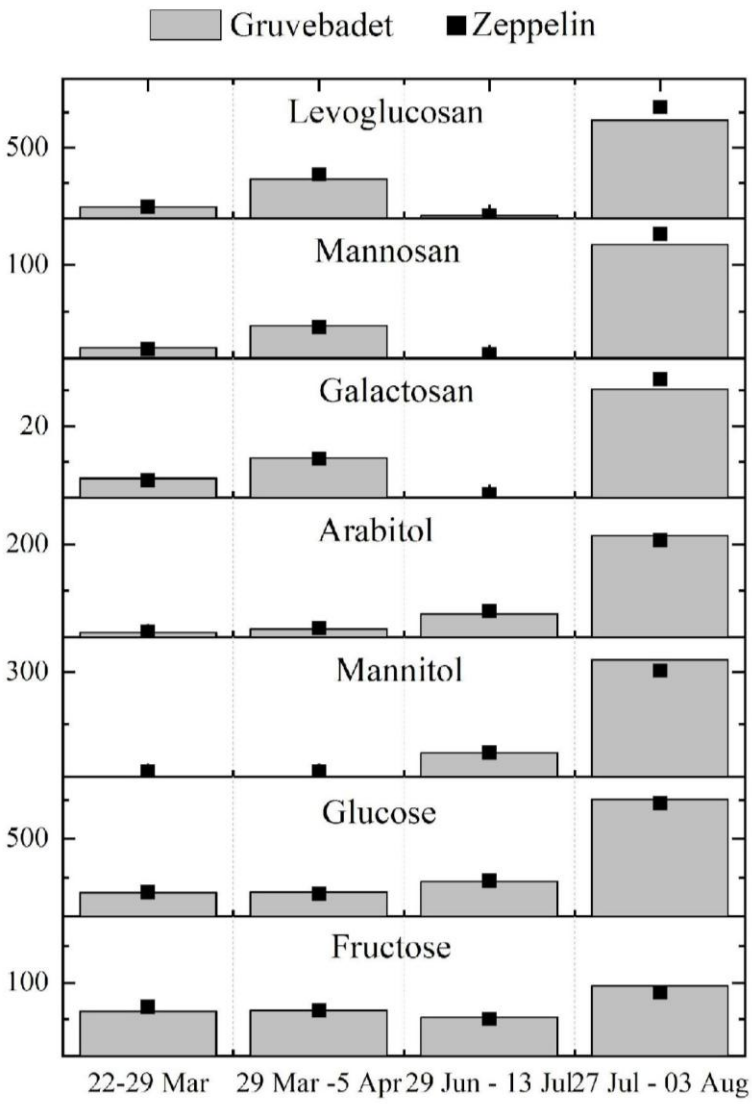


Figure S14: Intercomparison exercise in which the Venice Lab quantified the same samples collected at ZEP using its own method. The results were also determined by NILU for comparison.

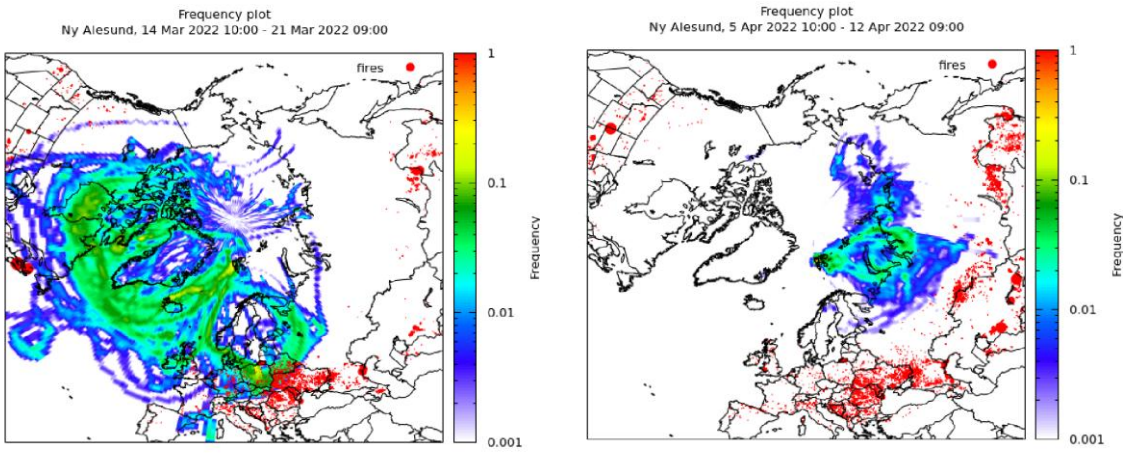


Figure S15: Frequency plot (note the logarithmic scale) for trajectories reaching the site from 10:00 of Mar 14 to 9:00 of Mar 21, 2022 (left hand side panel) and from 10:00 of 5 Apr to 9:00 12 Apr 2022 (right hand side panel). Fires from Modis are represented as red circles whose diameter is proportional to the fire radiative power.

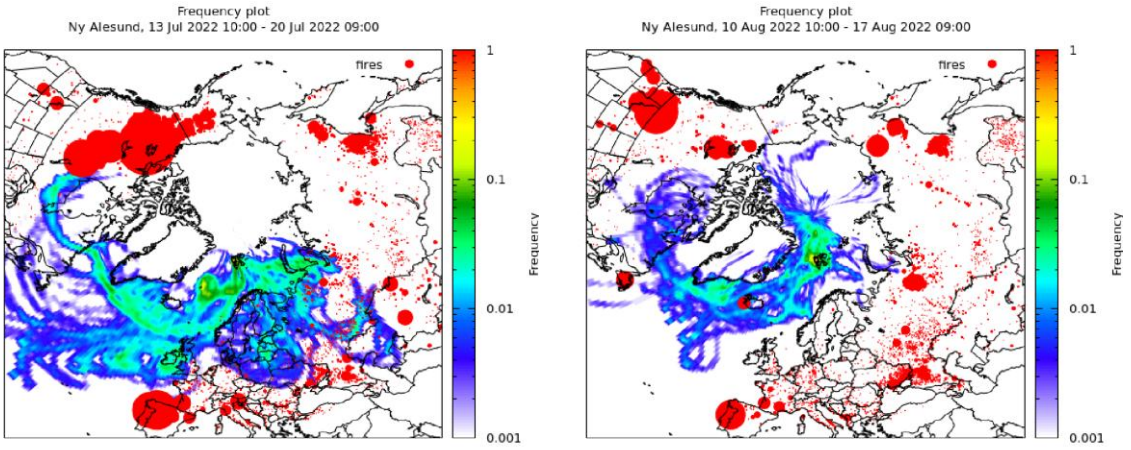


Figure S16: Frequency plot (note the logarithmic scale) for trajectories reaching the site from 10:00 of Jul 13 to 9:00 of Jul 20, 2022 (left hand side panel) and from 10:00 of 10 Aug to 9:00 17 Aug 2022 (right hand side panel). Fires from Modis are represented as red circles whose diameter is proportional to the fire radiative power.

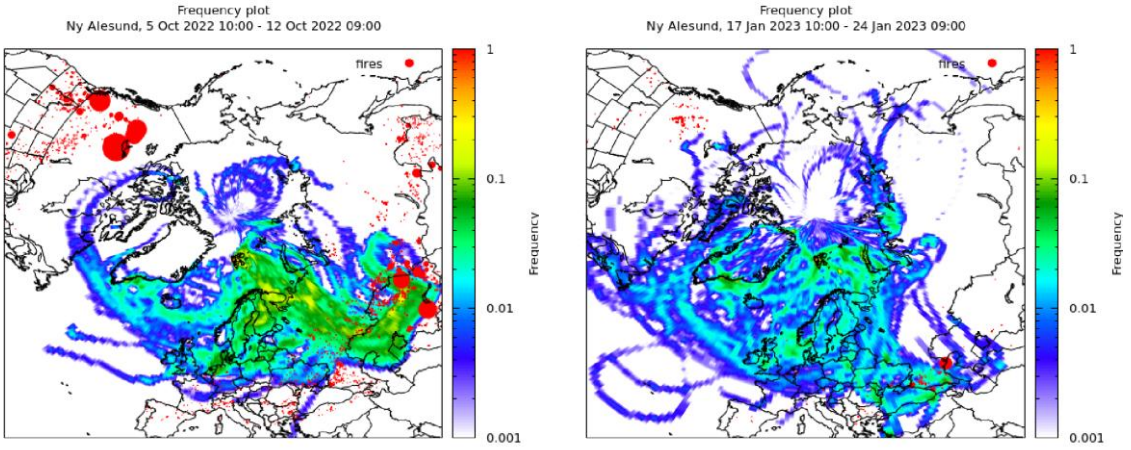


Figure S17: Frequency plot (note the logarithmic scale) for trajectories reaching the site from 10:00 of Oct 5 to 9:00 of Oct 12, 2022 (left hand side panel) and from 10:00 of 17 Jan to 9:00 24 Jan 2023 (right hand side panel). Fires from Modis are represented as red circles whose diameter is proportional to the fire radiative power.

Table S3. Percent of variance obtained by Partial Least Squares Discriminant Analysis (PLS-DA) where X represents 30 variables (compounds) and Y defines the sites classification.

Number of Factors	Variance Explained for X Effects (%)	Cumulative X Variance (%)	Variance Explained for Y Responses (%)	Cumulative Y Variance (%)
1	29.5	29.5	39.9	39.9
2	8.3	37.7	21.2	61.2
3	8.6	46.3	5.4	66.6
4	9.6	56.0	2.0	68.6
5	4.6	60.6	3.9	72.6
6	9.6	70.2	1.5	74.0
7	5.7	75.9	1.2	75.3
8	3.5	79.3	0.8	76.1
9	1.3	80.7	1.8	77.8
10	2.3	83.0	0.5	78.3
11	3.1	86.1	0.2	78.6
12	1.7	87.7	0.2	78.8
13	2.4	90.2	0.1	78.8
14	1.2	91.3	0.1	78.9
15	1.6	92.9	0.0	79.0

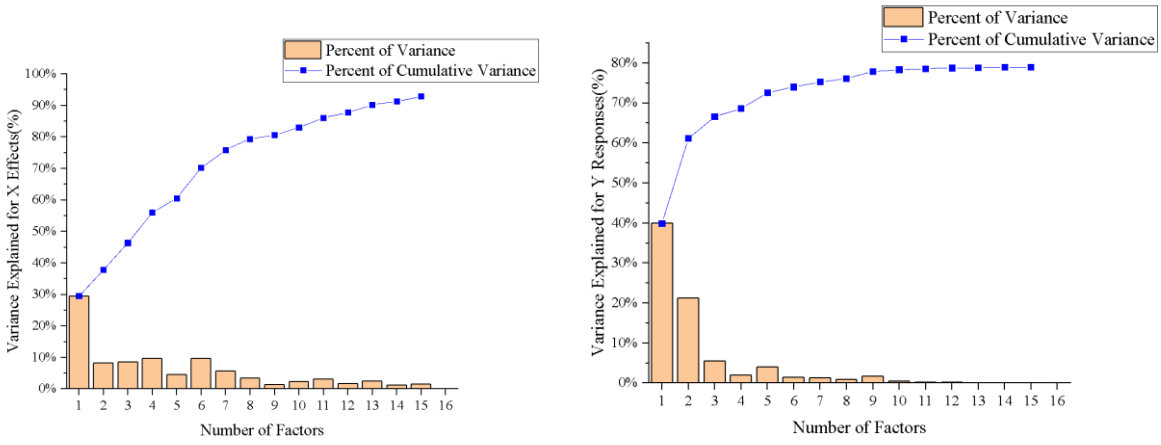


Figure S18. Percent of variance obtained by Partial Least Squares Discriminant Analysis (PLS-DA) where X represents 30 variables (compounds) and Y defines the sites classification.